

Electric field tunable non-linear Hall terahertz detector in Dual quantum spin Hall insulator TaIrTe₄

Junwen Lai,^{1,2} Jie Zhan,^{1,2} Peitao Liu,^{1,2} Xing-Qiu Chen,^{1,2,*} and Yan Sun^{1,2,†}

¹*School of Materials Science and Engineering, University of Science and Technology of China, Shenyang 110016, China.*

²*Shenyang National Laboratory for Materials Science, Institute of Metal Research, Chinese Academy of Sciences, Shenyang 110016, China.*

Nonlinear Hall effect (NHE) can be generated via Berry curvature dipole (BCD) on nonequilibrium Fermi surface in a non-magnetic system without inversion symmetry. To achieve a large BCD, strong local Berry curvatures and their variation with respect to momentum are necessary and hence topological materials with strong inter-band coupling emerge as promising candidates. In this study, we propose a switchable and robust BCD in the newly discovered dual quantum spin Hall insulator (QSHI) TaIrTe₄ by applying out-of-plane electric fields. Switchable BCD could be found along with topological phase transitions or insulator-metal transition in the primitive cell and CDW phases of TaIrTe₄ monolayer. This work presents an instructive strategy for achieving a switchable and robust BCD within dual QSHIs, which should be helpful for designing the NHE-based THz radiations detector.

I. INTRODUCTION

In nonlinear second-order quantum responses, the Berry curvature dipole (BCD) has recently attracted much attention as it could widely occur in non-magnetic systems with breaking inversion symmetry at both zero and twice driving frequency[1, 2]. Unlike the well-known anomalous Hall effect (AHE) which serves as a summation of Berry curvature, BCD manifests as a spatially varying distribution of Berry curvature in momentum space and does not require time reversal symmetry broken. In the last decades, BCD has provided inspirations in many physical properties and applications including spintronics, energy harvesting and microwave detection [3–15]. Very recently, the utilization of BCD as a rectifier of terahertz (THz) wave provides a new strategy for the THz radiation detection based on intrinsic electronic band structures in materials[10], see Fig. 1. The THz technology is making groundbreaking advancement and has already been proposed as a next-generation technology in many fields including spectroscopy, sensing, information and communication[16, 17]. Despite these wide potentials, its practical application as THz detection still faces challenges in obtaining a sensitive, switchable, and significant signal, as well as the compatibility to integral into currently using electronic devices. Therefore, new design of the devices and materials candidates are desired.

Materials with high BCD have been studied in various systems including topological insulators (TIs), Weyl semimetals (WSMs), transition metal dichalcogenides, anti-ferromagnetic metals, etc., both theoretically and experimentally [4–15]. Topological materials are naturally with great potential to have large BCD due to their large local Berry curvature originating from the

band inversion. The electric field serves as an effective method to tune the electronic structures and induce phase transition in two-dimensional (2D) topological materials[7, 13, 15, 18, 19]. Therefore, tunable NHE in 2D topological materials is expected in the condition with gating fields. The experimental studies about BCD in 2D TIs are rare due to the lack of promising material candidates. Most studies focus on transition metal dichalcogenides WTe₂/MoTe₂ and the moiré superlattice[4, 6, 7, 13].

Very recently, a new topological phase of dual quantum spin Hall insulator (QSHI) was discovered in TaIrTe₄[20] monolayer. In addition to the nontrivial band gap at the charge neutrality points[21, 22], a new Z_2 gap can be generated when the chemical potential shifts to the van Hove singularity (VHS) point, which reveals strong inter-band coupling in a large energy window. In this work, the electronic structure and topological phase transition of this new phase are studied in detail. Based on the electronic structure evolution, we calculated its switchable non-linear Hall performance under a varying electric field. Taking advantage of the switchable NHE and large current responsivity in monolayer TaIrTe₄, a BCD based Hall rectifier could be designed and utilized in the AC electrical fields and THz radiation detection.

II. METHOD

A. Non-linear Hall effect

Consider two linear polarized THz radiations or AC electric fields defined by $\varepsilon_b(t) = \varepsilon_b e^{i\omega t}$ and $\varepsilon_c(t) = \varepsilon_c e^{i\omega t}$, where b and c are the polarized direction and ω is the wave frequency. The non-linear Hall rectify current along a direction is given by[1]

$$j_a = \chi_{abc} \varepsilon_b \varepsilon_c^* \quad (1)$$

By considering the symmetry of this second-order tensor and ignoring the conductivity coefficient, it's convenient

* xingqiu.chen@imr.ac.cn

† sunyan@imr.ac.cn

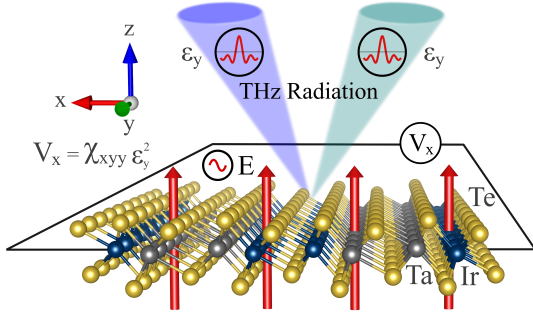


FIG. 1. Schematic view of terahertz (THz) photodetection based on the Berry curvature dipole (BCD) of the quantum spin Hall insulator (QSHI) TaIrTe₄. ε_y is the amplitude of the THz polarized light along y direction, j_x is the non-linear DC current along x direction, E is the electric field perpendicular to the monolayer TaIrTe₄. The strength of this mechanism could be described by the nonlinear conductivity χ_{xyy} .

to reform χ_{abc} into a two-indices quantity D_{bd} . Besides, only z component of Berry curvature exists for 2D material. Thus, only components with $d = z$ and $a, c = x, y$ can exist, which reads

$$\chi_{xyy} = -\chi_{yyx} = \frac{e^3 \tau}{2\hbar^2(1 + i\omega\tau)} D_{bz} \quad (2)$$

$$D_{bz} = \int [d\mathbf{k}] \sum_n f_{n\mathbf{k}} \frac{\partial \Omega_{z\mathbf{k}}^n}{\partial k_b} \quad (3)$$

where τ is the electron relaxation time, and $f_{n\mathbf{k}} = 1/(e^{(E_{n\mathbf{k}} - E_f - \mu)/\epsilon} + 1)$ is the Fermi-Dirac distribution under the equilibrium state. $\Omega_{z\mathbf{k}}^n$ is the Berry curvature of the n -th band at momenta \mathbf{k} , which reads

$$\Omega_{z\mathbf{k}}^n = 2i\hbar^2 \sum_{m \neq n} \frac{\langle u_{n\mathbf{k}} | \hat{v}_x | u_{m\mathbf{k}} \rangle \langle u_{m\mathbf{k}} | \hat{v}_y | u_{n\mathbf{k}} \rangle}{(E_{n\mathbf{k}} - E_{m\mathbf{k}})^2} \quad (4)$$

where $\hat{v}_a = \frac{1}{\hbar} \frac{\partial \hat{H}}{\partial k_a}$ is the velocity operator along a direction, \hat{H} is the Hamiltonian in Wannier basis, $|u_{n\mathbf{k}}\rangle$ is the eigenstate of Hamiltonian with the eigenvalue of $E_{n\mathbf{k}}$. Note that the BCD is unit-free in three-dimension and with a unit of Angstrom in 2D.

Considering the scattering rate of electrons is in the order of tens of THz, the NHE in materials can be utilized in rectifying incident THz radiations with the output of direct electrical current. Corresponding performance of the THz detector device can be characterized by the strength of the electric output per optical input, which is known as the current responsivity[10]. To obtain it, the power of the Hall rectifier P should also be taken into consideration other than the BCD, which reads

$$P = \frac{e\tau}{\hbar(1 + i\omega\tau)} \sigma_{ab} \varepsilon_a \varepsilon_b LW \quad (5)$$

where L and W are the length and width of the Hall rectifier. σ_{ab} is the Drude weight, which is given by

$$\begin{aligned} \sigma_{ab} &= \frac{e}{\hbar} \int [d\mathbf{k}] \frac{\partial E}{\partial k_a} \frac{\partial E}{\partial k_b} \left(-\frac{\partial f_{\mathbf{k}}}{\partial E} \right) \\ &= \frac{e}{\hbar} \int [d\mathbf{k}] \sum_n \langle n | \hat{v}_a | n \rangle \langle n | \hat{v}_b | n \rangle \delta(E_{\mathbf{k}} - E_n) \end{aligned} \quad (6)$$

Thus, the current responsivity R_a of the Hall rectifier could be given by the output current per adsorbed power which reads

$$R_a = \frac{I_H}{P} = \frac{1}{W} \frac{D_{az}}{\hbar \sigma_{aa}} \quad (7)$$

where the term of $\tau/(1+i\omega\tau)$ with electron relaxation time is canceled out.

The monolayer TaIrTe₄ belongs to a centrosymmetric space group $P2_1/m$, where nonlinear response is forbidden due to the inversion symmetry. After applying an electric field perpendicular to the layer, this inversion symmetry is broken and only a mirror symmetry $\{\mathcal{M}_y | (0, 1/2, 0)\}$ is preserved. This symmetry leads to an odd $\frac{\partial \Omega_z}{\partial k_x}$ and an even $\frac{\partial \Omega_z}{\partial k_y}$. Therefore, only the components with $b = y$ (D_{yz} , χ_{xyy} , χ_{yyx} , σ_{yy} and R_y) are allowed to exist. The numerical integration over the whole Brillouin zone (BZ) is performed on a dense k -grid of 2000×2000 and 500×500 for the primitive cell and CDW phase of the monolayer TaIrTe₄ respectively and are tested to be fully coverage for both BCD and Drude term. Wilson loop is carried out in Wannier basis to characterize the Z_2 topological charges of TaIrTe₄ under different electric fields[23].

B. Ground state calculation

The crystal structure of the monolayer TaIrTe₄ is fully optimized with force difference on each atom no more than 0.001 eV/Å in Vienna Ab Initio Simulation Package (VASP)[24, 25] and in good agreement with experimental reports[20, 26]. Ground state calculation is performed in Full Potential Localized-orbital (FPLO) program to obtain a symmetry conserved Hamiltonian in Wannier basis[27–30]. The electric field is simulated by adding an on-site energy which varies linearly with the Wannier center coordinates perpendicular to the 2D plane on the Hamiltonian in Wannier basis. The Hamiltonian of the $15 \times 1 \times 1$ supercell is built from the hopping strength extracted from the Wannier function of the primitive cell. The CDW phase is simulated by a superlattice modulation of Fröhlich-Peierls Hamiltonian of $H = H_r + V \cos(Qx) u_r^\dagger u_r$, where V is the CDW modulation strength, Q is the magnitude of the CDW vector and x is the Wannier center coordinate along x axis[23, 31].

III. RESULTS AND DISCUSSION

A. Electronic structure of monolayer TaIrTe₄

The electronic band structure of monolayer TaIrTe₄ is shown in Fig. 2(b), where all the bands are doubly degenerate due to the inversion symmetry. From energy dispersion we can find a band inversion near Γ point, which corresponds to a QSHI phase with a band gap of around 45 meV, in agreement with the previous reports[20–22]. After applying an electric field along z , the inversion symmetry is broken and leads to a band splitting between spin-up and spin-down channels, see Fig. 2(c-f). This band splitting gradually grows as the electric field increases. Meanwhile, the band gap along S - X gradually decreases and gets crossed when the field reaches around 1.0 eV/c, see Fig. 2(d). After the crossing, the band gap is reformed and the monolayer TaIrTe₄ becomes a trivial insulator with a band gap of around 13 meV($E=2.0$ eV/c).

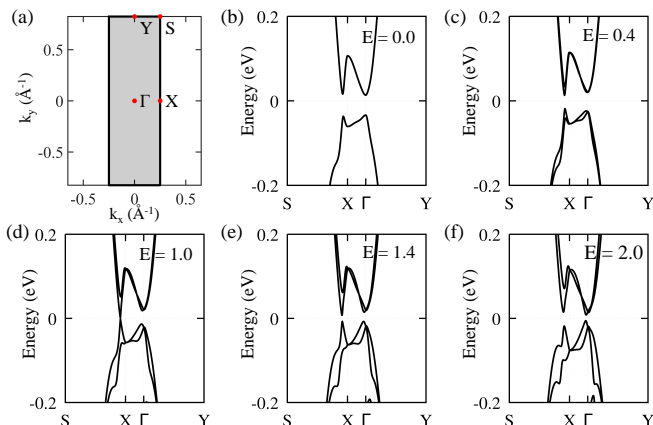


FIG. 2. (a) Brillouin Zone (BZ) of TaIrTe₄ monolayer; (b-f) Energy dispersions of TaIrTe₄ monolayer with different electric fields E . E is given in the unit of eV/c, with $c = 4.010 \text{ \AA}$ as the layer thickness of TaIrTe₄ monolayer.

B. Non-linear Hall effect in monolayer TaIrTe₄

The above band structure analysis demonstrates the inversion symmetry broken after applying an out-of-plane field, which is essential for generating a non-linear response. Besides, topological phase transitions would happen for some given electric fields. Since such phase transitions are often along with dramatic changes in Berry curvature distribution, we analyzed corresponding non-linear Hall transport in detail, see Fig. 3. In the absence of the electric field, the BCD is forced to zero due to the inversion symmetry (black line). After applying a small electric field of $E = 0.4$ eV/c, the D_{yz} component of BCD increases sharply from zero, consistent with our symme-

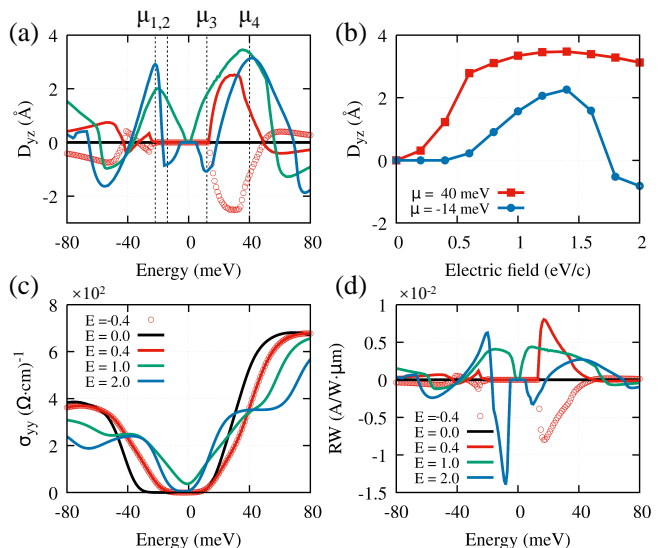


FIG. 3. (a) Chemical potential dependent BCD of TaIrTe₄ monolayer at different electric fields. Four peaks can be found near the Fermi energy, with $\mu_1 = -22$ meV, $\mu_2 = -14$ meV, $\mu_3 = 12$ meV, $\mu_4 = 40$ meV. (b) The BCD of TaIrTe₄ monolayer at chemical potentials of μ_2 and μ_4 with varying electric fields. (c) The chemical potential dependent Drude weight σ_{yy} of TaIrTe₄ monolayer at different electric fields. (d) The chemical potential dependent current responsivity times width (RW) of TaIrTe₄ monolayer with different electric fields.

try analysis. Besides, a peak with the magnitude of 2.4 \AA can be found at the chemical potential of 40 meV (red line).

As the field continually increases to 1.0 eV/c, a phase transition from QSHI to normal insulator happens. Meanwhile, a new peak appears at around μ_1 and the peak at μ_4 becomes larger (green line). This can be attributed to the strength of inversion symmetry breaking induced by the electric field. After the phase transition when the electric field reaches around 2.0 eV/c (blue line), two peaks at μ_2 and μ_3 appear with opposite signs with respect to that at μ_1 and μ_4 .

To have a further understanding of the tunability of BCD, we analyzed the field dependent D_{yz} at given chemical potentials of μ_2 and μ_4 , respectively, see Fig. 3(b). For the behavior away from Fermi energy (μ_4), the change of D_{yz} is trivial as it increases monotonically up to 1.0 eV/c and saturates at around 3.5 \AA . Meanwhile, for the case near Fermi energy (μ_2), the rate of increase in D_{yz} slows down at 1.0 eV/c and subsequently decreases rapidly after 1.4 eV/c, resulting in a sign change at 1.6 eV/c. This indicates the emergence of some negative contribution after the topological phase transition. Besides, the magnitude of this negative contribution increases much faster than the positive counterpart with the increasing electric field, resulting in a sign change near the Fermi energy.

To obtain the absorbed power of the THz Hall rectifier,

we also calculated the Drude term σ_{yy} , see Fig. 3(c). Due to the intra-band Drude term, a zero plateau emerges within the band gap near the Fermi level. The magnitude of σ_{yy} grows rapidly as it gets away from the gap. When an electric field is applied, the basic shape of σ_{yy} is generally kept, and changes mainly occur in the zero plateau range and the curve broadening. Thus, the current responsivity R becomes larger near the band edge as it varies inversely with the absorbed power σ_{yy} . This can be confirmed by the analysis of the RW plot in Fig. 3(d). Although the magnitude of the BCD peak near μ_2 is smaller compared to the peak at μ_1 , the current responsivity exhibits distinct behavior, as the peak near μ_1 demonstrates greater robustness and tunability.

The intensity of RW could reach around 1.4×10^{-2} $\mu\text{m}/\text{V}$, indicating the potential to get a current responsivity R of 0.14 V^{-1} with a sample width of $0.1 \mu\text{m}$. Taking advantage of the controllable growth nature of 2D materials, a smaller sample width can be achieved to yield a stronger signal. Additionally, the direction of the nonlinear Hall current can be flipped by the sign of the applied electric field, as illustrated in the comparison between the red solid and dot curves in Fig. 3(a,b,d).

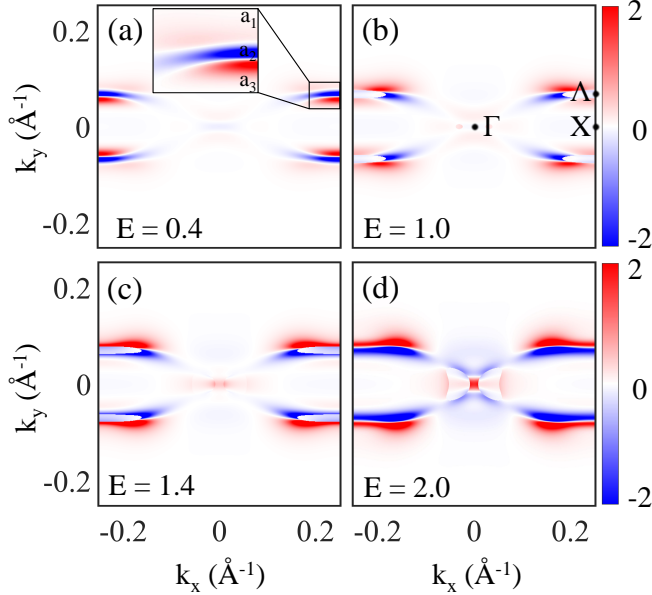


FIG. 4. The Berry curvature dipole distribution $\tilde{D}_{yz\mathbf{k}} = \sum_n \frac{f_n \mathbf{k}}{V} \frac{\partial \Omega_{z\mathbf{k}}^n}{\partial k_y}$ under different electric fields of (a) $E = 0.4 \text{ eV}/c$, (b) $E = 1.0 \text{ eV}/c$, (c) $E = 1.4 \text{ eV}/c$, and (d) $E = 2.0 \text{ eV}/c$ with a given chemical potential $\mu_2 = -14 \text{ meV}$. BZ along k_y axis is zoomed in as the other part is negligible, colorbars of $\tilde{D}_{yz\mathbf{k}}$ are all in unit of 10^4 .

To understand the sign change of BCD under different electric fields and chemical potentials, we analyzed the local distribution $\tilde{D}_{yz\mathbf{k}}$ and $\tilde{\Omega}_{z\mathbf{k}}$, see Figs. 4 and 5. Since the Fermi crossing mainly takes place near the $k_y = 0$ line, the non-zero BCD distribution is confined in the range of k_y between -0.25 and 0.25 \AA^{-1} , see Figs. 2 and 4.

Applying an electric field, a sign change at the chemical potential $\mu_2 = -14 \text{ meV}$ could be found. The detailed local distribution of $\tilde{D}_{yz\mathbf{k}}$ at $\mu_2 = -14 \text{ meV}$ is shown in Fig. 4. For the $\tilde{D}_{yz\mathbf{k}}$ under a small electric field of $E = 0.4 \text{ eV}/c$, the high intensities mainly locate near the Λ point, see Fig. 4(a).

For convenience, the dominant contribution is divided into three areas around the Λ point, where a_1 and a_3 exhibit positive dominance while a_2 is negative. With detailed quantitative analysis, we can see that a_1 and a_3 make a larger contribution compared to a_2 at low electric field, see Fig. 4(a), which results in the positive D_{yz} in Fig. 3(a). As the electric field increases, the magnitude of $\tilde{D}_{yz\mathbf{k}}$ in a_1 and a_3 grows and decays, respectively. Meanwhile, the magnitude in a_2 increases rapidly and eventually becomes dominated after the topological phase transition. The joint effect of the three areas explains why the sign change of D_{yz} is later than the topological phase transition.

The chemical potential-dependent BCD is also analyzed at a given $E = 2.0 \text{ eV}/c$, see Fig. 5. Both local Berry curvature $\tilde{\Omega}_{z\mathbf{k}}$ (Fig. 5(a-d)) and BCD $\tilde{D}_{yz\mathbf{k}}$ (Fig. 5(e-h)) of the four peaks in Fig. 3 are calculated. Owing to the mirror plane of $\{\mathcal{M}_y | (0, 1/2, 0)\}$, $\tilde{\Omega}_{z\mathbf{k}}$ is even with respect to k_x and odd with respect to k_y under an out-of-plane electric field. Since BCD is a first-order derivative of the Berry curvature, it exhibits different parity characteristics compared to the Berry curvature with respect to momentum. Therefore, $\tilde{D}_{yz\mathbf{k}}$ presents as an even function of k_x and k_y , respectively, see Fig. 5(e-h).

With the above understanding of symmetry analysis, we go to the details about the Berry curvature distribution in k space, see in Fig. 5(a-d). As depicted in Fig. 5(a), two hot spots could be seen around Θ and Γ points in the positive BZ zone, which are negative and positive dominated, respectively. The three peaks of μ_1 - μ_3 in Fig. 3(a) share similar Berry curvature distributions, see the comparison of Fig. 5(a-c). Owing to the crossing of the conduction band, an empty part appears near the Θ point in Fig. 5(c). As a consequence, the distribution of $\tilde{D}_{yz\mathbf{k}}$ in Fig. 5(e-g) also shows a similar shape. The negative region in $\tilde{\Omega}_{z\mathbf{k}}$ splits into two areas with opposite signs in $\tilde{D}_{yz\mathbf{k}}$. The intensity of these areas differs as the negative part is stronger in μ_2 and μ_3 , which primarily contributes to the sign change of D_{yz} near the Fermi level. Besides, the magnitude of $\tilde{\Omega}_{z\mathbf{k}}$ around Γ is small and makes little contribution to the D_{yz} . As presented in Figs. 5(d) and (h), there are multiple band contributions at $\mu_4 = 40 \text{ meV}$, and they are mainly dominated by the positive intensity, leading to the corresponding peak in Fig. 3(a).

C. Non-linear Hall transport in CDW phase

Apart from the QSHI state at the charge neutrality point, a new Z_2 gap can be generated by placing the

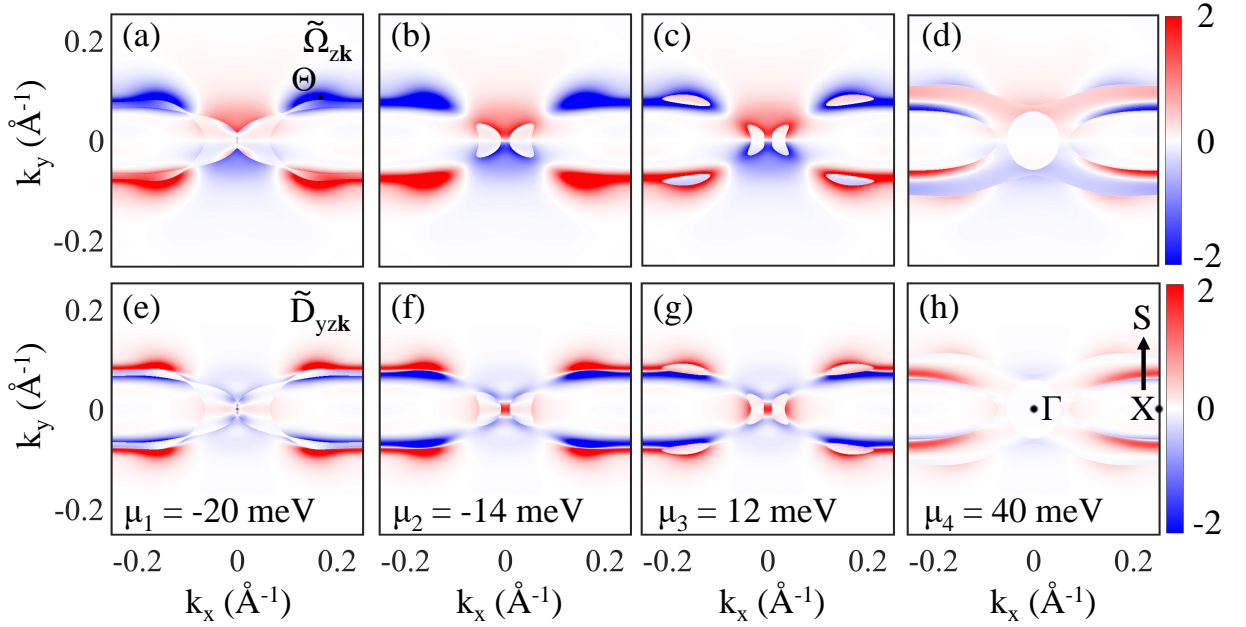


FIG. 5. The Berry curvature distribution $\tilde{\Omega}_{zk} = \sum_n f_{nk} \Omega_{zk}^n$ of TaIrTe₄ monolayer at different chemical potentials of (a) $\mu_1 = -22$ meV, (b) $\mu_2 = -14$ meV, (c) $\mu_3 = 12$ meV, and (d) $\mu_4 = 40$ meV under an electric field of $E = 2.0$ eV/c. The BCD distribution \tilde{D}_{yzk} of TaIrTe₄ monolayer at different chemical potentials of (e) $\mu_1 = -22$ meV, (f) $\mu_2 = -14$ meV, (g) $\mu_3 = 12$ meV, and (h) $\mu_4 = 40$ meV under an electric field of $E = 2.0$ eV/c. BZ along k_y axis is zoomed in as the other part is negligible, color bars of $\tilde{\Omega}_{zk}$ and \tilde{D}_{yzk} are in unit of $10^2 \hbar/e^2(\text{\AA})$ and 10^4 , respectively.

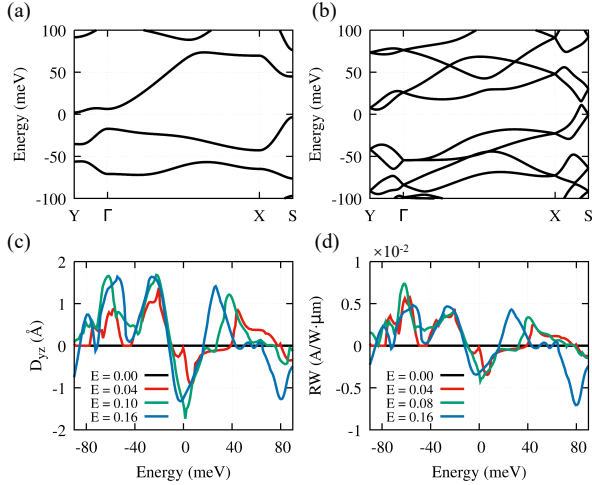


FIG. 6. (a) Band structure of the CDW phase TaIrTe₄ monolayer. (b) Band structure of the CDW phase TaIrTe₄ monolayer under an electric field of $E = 0.16$ eV/c. (c) The chemical potential dependent BCD of the CDW phase TaIrTe₄ monolayer at different electric fields. (d) The chemical potential dependent current responsivity times width (RW) of the CDW phase TaIrTe₄ monolayer at different electric fields.

Fermi level at van Hove singularity point. It has been reported that the CDW phase in monolayer TaIrTe₄ has a wave vector of $Q^* = (0.068, 0)$ [20]. With the inspiration

from experimental reports, we also computed the BCD and corresponding current responsivity near the CDW gap. According to the quantum electrical transport measurements, a periodic potential of $V = 0.13$ eV is taken into account to generate the CDW phase, see Fig. 6(a). Similar to the original primitive cell, all bands in Fig. 6(a) are doubly degenerated due to the inversion symmetry. Thus, an out-of-plane electric field is applied to induce the non-linear Hall response, see Fig. 6(b). As a result, a significant band split was induced under a small electric field of $E = 0.16$ eV/c (approximately 0.4 eV/nm), see Fig. 6(b). All three CDW gaps disappear along with the increasing of electric field.

With the guiding principle from band structures, we analyzed the non-linear Hall transport in detail. Multiple peaks of BCD and current responsivity can be found in Fig. 6(c,d) and they show similar trends under different electric fields. There are three clear peaks near the Fermi level. Two positive peaks with the magnitude of 1.67\AA are located at around -54 meV and -26 meV, respectively. While a negative peak of -1.31\AA is located at around -3 meV. These results suggest that the CDW phase of monolayer TaIrTe₄ can also be tuned by shifting the chemical potential near the CDW gap.

IV. CONCLUSION

In this work, we systemically studied the electronic structures and the non-linear Hall transports in the new discovered topological state of dual QSHI in TaIrTe₄. Strong peaks of BCD were identified in the condition of a gating electric field and found to be switchable in terms of both sign and magnitude. Through the analysis of momentum-resolved BCD, we reveal that the switchable phenomenons correspond precisely to the topological phase transition in both the primitive cell and CDW phase. The results from our calculations illustrate that the topological band gaps in dual QSHIs offer natural

platforms to obtain strong and tunable NHE and they exhibit promising potential applications in the next generation of THz radiation detection technologies.

ACKNOWLEDGMENTS

This work is supported by the National Key R&D Program of China 2021YFB3501503, National Natural Science Foundation of China (Grants No.52271016, No.52188101), and Liaoning Province (Grant No. XLYC2203080). Part of the numerical calculations in this study were carried out on the ORISE Supercomputer(No. DFZX202319).

-
- [1] I. Sodemann and L. Fu, “Quantum nonlinear hall effect induced by berry curvature dipole in time-reversal invariant materials,” *Phys. Rev. Lett.*, vol. 115, p. 216806, Nov. 2015.
- [2] Z. Z. Du, H.-Z. Lu, and X. C. Xie, “Nonlinear Hall effects,” *Nature Reviews Physics*, vol. 3, pp. 744–752, Nov. 2021.
- [3] D. Xiao, M.-C. Chang, and Q. Niu, “Berry phase effects on electronic properties,” *Rev. Mod. Phys.*, vol. 82, pp. 1959–2007, July 2010.
- [4] J.-S. You, S. Fang, S.-Y. Xu, E. Kaxiras, and T. Low, “Berry curvature dipole current in the transition metal dichalcogenides family,” *Phys. Rev. B*, vol. 98, p. 121109(R), Sept. 2018.
- [5] Y. Zhang, Y. Sun, and B. Yan, “Berry curvature dipole in Weyl semimetal materials: An ab initio study,” *Phys. Rev. B*, vol. 97, p. 041101(R), Jan. 2018.
- [6] Y. Zhang, J. van den Brink, C. Felser, and B. Yan, “Electrically tuneable nonlinear anomalous Hall effect in two-dimensional transition-metal dichalcogenides WTe₂ and MoTe₂,” *2D Materials*, vol. 5, p. 044001, July 2018.
- [7] S.-Y. Xu, Q. Ma, H. Shen, V. Fatemi, S. Wu, T.-R. Chang, G. Chang, A. M. M. Valdivia, C.-K. Chan, Q. D. Gibson, J. Zhou, Z. Liu, K. Watanabe, T. Taniguchi, H. Lin, R. J. Cava, L. Fu, N. Gedik, and P. Jarillo-Herrero, “Electrically switchable Berry curvature dipole in the monolayer topological insulator WTe₂,” *Nature Physics*, vol. 14, pp. 900–906, Sept. 2018.
- [8] C. Wang, Y. Gao, and D. Xiao, “Intrinsic nonlinear hall effect in antiferromagnetic tetragonal CuMnAs,” *Phys. Rev. Lett.*, vol. 127, p. 277201, Dec. 2021.
- [9] P. A. Pantaleón, T. Low, and F. Guinea, “Tunable large Berry dipole in strained twisted bilayer graphene,” *Phys. Rev. B*, vol. 103, p. 205403, May 2021.
- [10] Y. Zhang and L. Fu, “Terahertz detection based on nonlinear Hall effect without magnetic field,” *Proceedings of the National Academy of Sciences*, vol. 118, p. e2100736118, May 2021.
- [11] S. Sinha, P. C. Adak, A. Chakraborty, K. Das, K. Debnath, L. D. V. Sangani, K. Watanabe, T. Taniguchi, U. V. Waghmare, A. Agarwal, and M. M. Deshmukh, “Berry curvature dipole senses topological transition in a moiré superlattice,” *Nature Physics*, vol. 18, pp. 765–770, July 2022.
- [12] Q. Fu, X. Cong, X. Xu, S. Zhu, X. Zhao, S. Liu, B. Yao, M. Xu, Y. Deng, C. Zhu, X. Wang, L. Kang, Q. Zeng, M.-L. Lin, X. Wang, B. Tang, J. Yang, Z. Dong, F. Liu, Q. Xiong, J. Zhou, Q. Wang, X. Li, P.-H. Tan, B. K. Tay, and Z. Liu, “Berry Curvature Dipole Induced Giant Mid-Infrared Second-Harmonic Generation in 2D Weyl Semiconductor,” *Advanced Materials*, vol. 35, p. 2306330, Nov. 2023.
- [13] X.-G. Ye, H. Liu, P.-F. Zhu, W.-Z. Xu, S. A. Yang, N. Shang, K. Liu, and Z.-M. Liao, “Control over berry curvature dipole with electric field in WTe₂,” *Phys. Rev. Lett.*, vol. 130, p. 016301, Jan. 2023.
- [14] S. Duan, F. Qin, P. Chen, X. Yang, C. Qiu, J. Huang, G. Liu, Z. Li, X. Bi, F. Meng, X. Xi, J. Yao, T. Ideue, B. Lian, Y. Iwasa, and H. Yuan, “Berry curvature dipole generation and helicity-to-spin conversion at symmetry-mismatched heterointerfaces,” *Nature Nanotechnology*, vol. 18, pp. 867–874, Aug. 2023.
- [15] K. Lempicka Mirek, M. Król, H. Sigurdsson, A. Wincukiewicz, P. Morawiak, R. Mazur, M. Muszyński, W. Piecek, P. Kula, T. Stefaniuk, M. Kamińska, L. D. Marco, P. G. Lagoudakis, D. Ballarini, D. Sanvitto, J. Szczytko, and B. Pietka, “Electrically tunable berry curvature and strong light-matter coupling in liquid crystal microcavities with 2d perovskite,” *Science Advances*, vol. 8, no. 40, p. eabq7533, 2022.
- [16] M. Tonouchi, “Cutting-edge terahertz technology,” *Nature Photonics*, vol. 1, pp. 97–105, Feb. 2007.
- [17] R. I. Stantchev, X. Yu, T. Blu, and E. Pickwell-MacPherson, “Real-time terahertz imaging with a single-pixel detector,” *Nature Communications*, vol. 11, p. 2535, May 2020.
- [18] J. Maciejko, T. L. Hughes, and S.-C. Zhang, “The quantum spin hall effect,” *Annual Review of Condensed Matter Physics*, vol. 2, no. Volume 2, 2011, pp. 31–53, 2011.
- [19] S. Wu, V. Fatemi, Q. D. Gibson, K. Watanabe, T. Taniguchi, R. J. Cava, and P. Jarillo-Herrero, “Observation of the quantum spin Hall effect up to 100 kelvin in a monolayer crystal,” *Science*, vol. 359, pp. 76–79, Jan. 2018.
- [20] J. Tang, T. S. Ding, H. Chen, A. Gao, T. Qian, Z. Huang, Z. Sun, X. Han, A. Strasser, J. Li, M. Geiwitz, M. Shehabeldin, V. Belosevich, Z. Wang, Y. Wang, K. Watanabe, T. Taniguchi, D. C. Bell, Z. Wang, L. Fu, Y. Zhang,

- X. Qian, K. S. Burch, Y. Shi, N. Ni, G. Chang, S.-Y. Xu, and Q. Ma, “Dual quantum spin Hall insulator by density-tuned correlations in TaIrTe_4 ,” *Nature*, Mar. 2024.
- [21] J. Liu, H. Wang, C. Fang, L. Fu, and X. Qian, “Van der Waals Stacking-Induced Topological Phase Transition in Layered Ternary Transition Metal Chalcogenides,” *Nano Lett.*, vol. 17, pp. 467–475, Jan. 2017.
- [22] P.-J. Guo, X.-Q. Lu, W. Ji, K. Liu, and Z.-Y. Lu, “Quantum spin Hall effect in monolayer and bilayer TaIrTe_4 ,” *Phys. Rev. B*, vol. 102, p. 041109(R), July 2020.
- [23] R. Yu, X. L. Qi, A. Bernevig, Z. Fang, and X. Dai, “Equivalent expression of Z_2 topological invariant for band insulators using the non-Abelian Berry connection,” *Phys. Rev. B*, vol. 84, p. 075119, Aug. 2011.
- [24] G. Kresse and J. Furthmüller, “Efficiency of ab-initio total energy calculations for metals and semiconductors using a plane-wave basis set,” *Comput. Mater. Sci.*, vol. 6, pp. 15–50, July 1996.
- [25] G. Kresse and J. Furthmüller, “Efficient iterative schemes for ab initio total-energy calculations using a plane-wave basis set,” *Phys. Rev. B*, vol. 54, pp. 11169–11186, Oct. 1996.
- [26] A. Mar, S. Jobic, and J. A. Ibers, “Metal-metal vs tellurium-tellurium bonding in WTe_2 and its ternary variants TaIrTe_4 and NbIrTe_4 ,” *Journal of the American Chemical Society*, vol. 114, no. 23, pp. 8963–8971, 1992.
- [27] K. Koepnick and H. Eschrig, “Full-potential nonorthogonal local-orbital minimum-basis band-structure scheme,” *Phys. Rev. B*, vol. 59, pp. 1743–1757, Jan. 1999.
- [28] I. Opahle, K. Koepnick, and H. Eschrig, “Full-potential band-structure calculation of iron pyrite,” *Phys. Rev. B*, vol. 60, pp. 14035–14041, Nov. 1999.
- [29] K. Koepnick, O. Janson, Y. Sun, and J. van den Brink, “Symmetry-conserving maximally projected Wannier functions,” *Phys. Rev. B*, vol. 107, p. 235135, June 2023.
- [30] J. P. Perdew, K. Burke, and M. Ernzerhof, “Generalized gradient approximation made simple,” *Phys. Rev. Lett.*, vol. 77, pp. 3865–3868, Oct. 1996.
- [31] H. Fröhlich, “On the theory of superconductivity: The one-dimensional case,” *Proceedings of the Royal Society of London. Series A. Mathematical and Physical Sciences*, vol. 223, no. 1154, pp. 296–305, 1954.